

Sedimentary structure of the western Bohai Bay basin and other basins in North China revealed by frequency dependent P-wave particle motion

Chenhao Yang*, Fenglin Niu

Department of Earth, Environmental and Planetary Sciences, Rice University, 6100 Main St, Houston, TX, 77005, USA



ARTICLE INFO

Article history:

Received 20 December 2017

Received in revised form

2 March 2018

Accepted 3 April 2018

Available online 27 September 2018

Keywords:

Teleseismic P wave

Nonlinear particle motion

Frequency-dependent

Sediment structure

Bohai Bay basin

ABSTRACT

High-resolution seismic models of sediment basins are critical inputs for earthquake ground motion prediction and petroleum resource exploration. In this study we employed a newly developed technique that utilizes the frequency-dependent nonlinear P-wave particle motion to estimate sedimentary structure beneath the Bohai Bay basin. A recent study suggests that the delay of the P wave on the horizontal component relative the vertical component and its variations over frequency are caused by interference of the direct P wave with waves generated at the sediment base. The frequency-dependent delay time can be used to constrain sediment thickness and seismic velocity beneath recording stations. We measured the particle motions of teleseismic P waves recorded by 249 broadband stations of the North China Array, which covers the western Bohai Bay basin and its surrounding areas. We found that the P waves of 90 stations inside the Bohai Bay basin and other local basins within the Taihang and Yanshan mountain ranges exhibit significant frequency-dependent nonlinear particle motions, and used the particle motion data to invert the sediment thickness (Z_0) and surface S-wave velocity (β_0). The estimated sediment thickness inside the Bohai Bay Basin varies from 1.02 km to 3.72 km, with an average of 3.20 km, which roughly agrees with previous active source studies.

© 2018 Institute of Seismology, China Earthquake Administration, etc. Production and hosting by Elsevier B.V. on behalf of KeAi Communications Co., Ltd. This is an open access article under the CC BY-NC-ND license (<http://creativecommons.org/licenses/by-nc-nd/4.0/>).

1. Introduction

The Bohai Bay basin, located inside the North China plain, is delimited by the Yanshan Mountains to the north, and the Taihang Mountains to west. It is also bordered by the Luxi uplift to the south and the Jiaodong and Liaodong uplifts to the east (Fig. 1). It comprises six relatively independent sub-basins: the Liaohe Depression (LHD) in the north-east, the offshore Bozhong Depression (BZD), the Jiyang Depression (JYD) and the Linqing-Dongpu Depression

(LDD) in the southeast, the Jizhong Depression (JZD) in the west, and the Huanghua Depression (HHD) in the central north (Fig. 1) [1]. The Bohai Baybasin also contains four major internal uplifts, which are Neihuang (NHU), Xingheng (XHU), Cangxian (CXU), and Chenning (CNU), which are located in the western part of the basin (Fig. 1).

The Bohai Bay basin is one of the most important oil and gas producing areas in China. Each sub-basin hosts at least one major oilfield of the Chinese oil industry. Over the last several decades, there were many 2D and 3D seismic surveys being conducted inside the basin, leading to significant insights on the sedimentary structure of the basin. The spatial coverage of 2D/3D seismic data is, however, still quite limited as compared to the full basin scale because of the high cost of data acquisition. Thus, there is still a demand to build a whole-basin scale 3D sedimentary model with good lateral resolution in order to delineate new areas of source reservoirs for future 2D/3D active exploration.

Sedimentary basins are formed through infilling of accommodation space, which created by long-term subsidence caused by

* Corresponding author.

E-mail address: cy15@rice.edu (C. Yang).

Peer review under responsibility of Institute of Seismology, China Earthquake Administration.



various tectonic processes, such as lithospheric stretching. The North China plain, which hosts the Bohai Bay basin, is located on the eastern part of the Sino-Korean craton with an Archean crust. This is the only large craton that is underlain by low seismic velocity at lithospheric depths in global tomography. Since the Mesozoic, the craton has undergone massive extension, which is likely caused by its interaction with subducting to the east – a situation similar to what has occurred in the western United States during the Cenozoic. Numerous mantle xenoliths from the region have already been studied indicating the deeper mantle portion of the continental lithosphere has been modified or even removed, probably sometime in the Mesozoic. To answer the question about the amount of lithosphere being removed in the past, it is essential to quantify the contribution of extension on lithospheric thinning. McKenzie [2] proposed an analytical model for the development and evolution of sedimentary basins due to stretching of continental lithosphere. He showed that there is quantitative relationship between the amount of extension and the volume of sediments as well as the changes in crustal thickness. Therefore, knowledge of the 3D sedimentary and crustal structure of the Bohai Bay basin can be used not only to unveil its formation mechanism, but also to understand regional tectonics.

The Bohai Bay basin and its surroundings are also known as earthquake prone areas in China [3]. Many devastating earthquakes occurred in the last century and before, such as the 1937 M7.0 Heze earthquake in Shandong province, the 1966 M7.2 Xingtai

earthquake and 1976 Tangshan earthquake in Hebei province. Knowing sedimentary structure within a basin is also of great importance to predict strong ground motions caused by earthquakes [4–6]. Unconsolidated sediments are formed by loose materials, ranging from clay to sand to gravel, and are usually featured by extremely low seismic velocity. Seismic waves entering the low-velocity sedimentary layer can be amplified and trapped, resulting in large ground shaking that can pose devastating damage to buildings and other infrastructures. The long-lasting large amplitude trapped waves or sediment reverberations also interfere with other seismic arrivals, making it difficult to isolate signals associated with deep structures from seismic records [7–9].

Bao and Niu [10] noticed that the primary P arrival times have a discrepancy between horizontal and vertical components for stations located inside sedimentary basins while the two arrival times should theoretically be the same since P wave is a body wave with a linear particle motion. They also found that the apparent P-wave (AP) splitting or nonlinear P-wave particle motion varies with frequency, which is caused by interference of the direct P wave with P-to-S conversion at the sediment base (hereafter referred to as Pbs) and sediment reverberations (Fig. 2). As the Pbs and multiples travel a very similar ray path before the conversion and reflection (Fig. 2a), their travel times are only slightly larger than that of the direct P wave. As shown in Fig. 2b, when the source pulse has a short duration, these arrivals are isolated. Meanwhile, the Pbs and multiples are largely registered on the radial (horizontal)

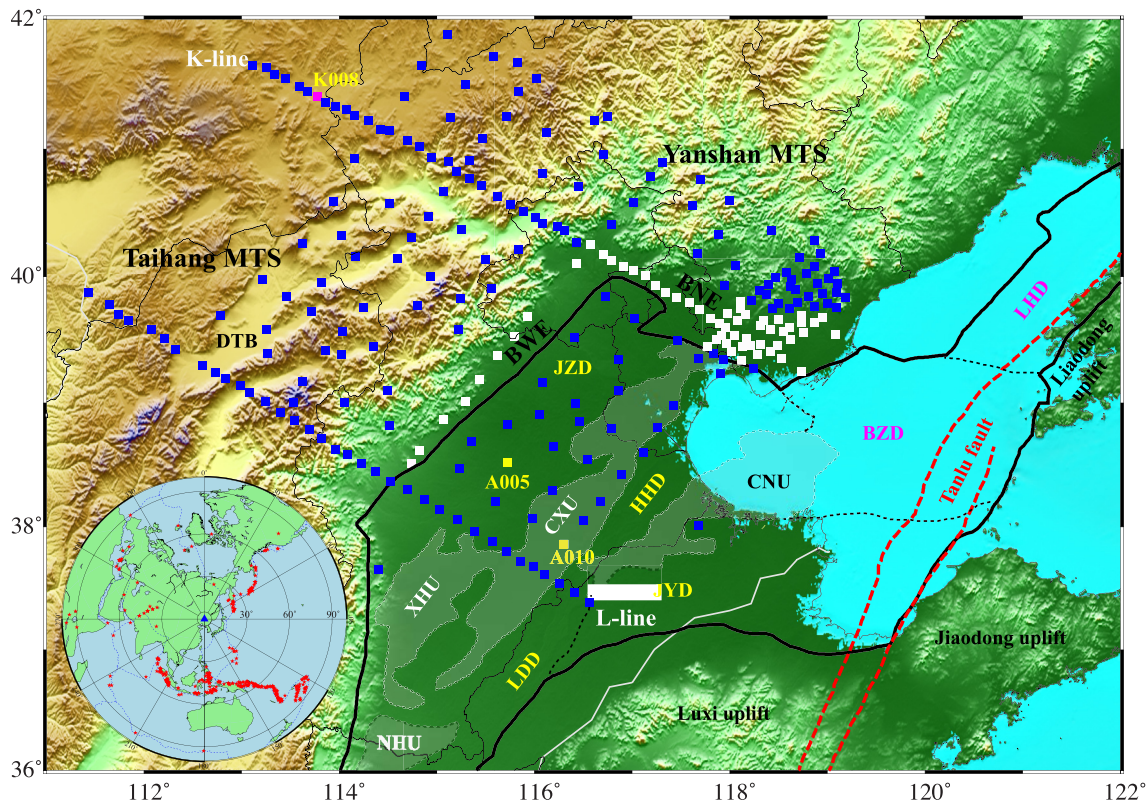


Fig. 1. Map showing the 249 broadband stations (solid squares) and the Tanlu fault (red dashed lines). The white squares denote stations that are located at low elevation areas outside the Bohai Bay Basin. The black solid line outlines the Bohai Bay Basin, which is composed of ten structural units bounded by dashed white lines: 1) LHD: the Liaohe Depression, 2) BZD: the Bozhong Depression, 3) CNU: the Chenning uplift, 4) JYD: the Jiyang Depression, 5) LDD: the Linqing-Dongpu Depression, 6) NHU: the Neihuang Uplift, 7) XHU: the Xingheng Uplift, 8) CXU: the Cangxian Uplift, 9) HHD: the Huanghua Depression, and 10) JZD: the Jizhong Depression. The northern and western margins of the Bohai Bay Basin are indicated by BNE and BWE, respectively. Inset shows the distribution of the 384 earthquakes (red stars) used in this study. The blue triangle indicates the center of the seismic array. Note that although the earthquakes seem to be $\sim 20^\circ$ – 100° away from the array center, we only choose stations in the epicentral distance range of 30° – 90° .

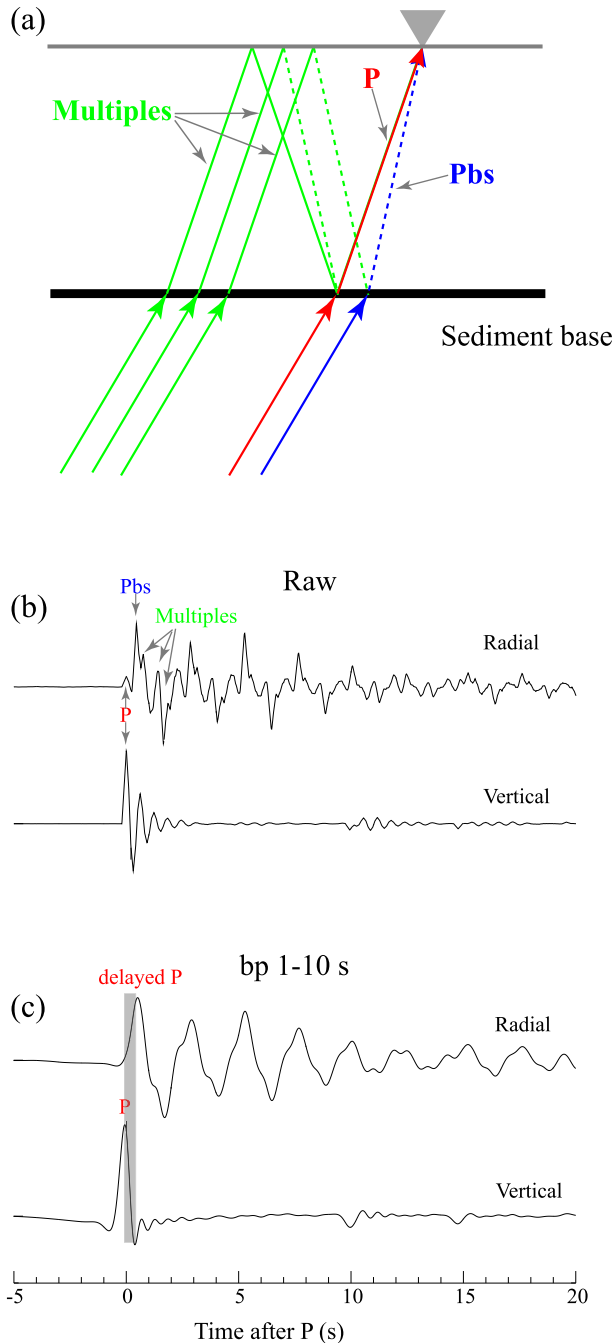


Fig. 2. (a) A schematic diagram showing the ray paths of the direct P wave (red line), P-to-S conversion at the bottom of the sediment (Pbs, blue line), and sediment multiples (green lines). P and S wave segments are shown in solid and dashed lines, respectively. (b) An example of the raw synthetic seismograms recorded on the radial and vertical components. Notice that the low-amplitude direct P wave on the radial component is closely followed by the high-amplitude converted wave and multiples. On the vertical component, P wave is the dominant arrival. Here since the source time function is a triangular function with short duration, therefore the P-wave and the later arrivals are separated. (c) The bandpass filtered records of (b). Note the interference caused an apparent delay of the P on the radial component.

component as they travel as an S wave along a nearly vertical path before reach to the station. On the vertical component, however, the direct P wave is still the dominant arrival (Fig. 2b). When the teleseismic records are bandpass filtered, the direct P wave and the

later arrivals interfere with each other, leading to an apparent delay of the first arrival in the radial component (Fig. 2c). It should be noted that a magnitude 5.8 earthquake has source time function with a duration of more than 4 s, therefore the direct P, Pbs and sediment multiples are never expected to show up as separate arrivals in a real seismogram. It is also worth noting that the apparent P wave splitting has nothing to do with seismic anisotropy inside the sediment and crust, although it is well known that S-wave splitting is generally caused by seismic anisotropy.

In this study, we apply their method to a large-scale broadband array temporarily deployed inside the Bohai Bay basin and its surrounding area. We first measure the frequency dependent apparent P-wave splitting times from a total of 249 broadband stations of the North China Array. We then employed the grid search technique to search for sediment thickness and S-wave velocity that best fit the observed splitting times. The inverted sediment model shows thick sediments with strong low-velocity anomalies at shallow depth of the Bohai Bay basin, and the lateral variation in sediment thickness being correlated well with the geographic locations of the sub-basins.

2. Data

We use teleseismic waveform data recorded by the North China Array (Fig. 1) deployed by the Institute of Geophysics, China Earthquake Administration (CEA) between October 2006 and July 2009 [11,12]. The 2D array forms a nearly square area of $\sim 375 \times 375$ km that covers a large part of the Bohai Bay basin, the Taihang Mountains and Yanshan Mountains. The station spacing is approximately 30 km. It also includes two dense survey lines with a station interval of ~ 10 km, which are denoted as K lines in the north and L line in the south. Most of the stations are equipped with a Guralp CMG-3ESPC seismometer and a Reftek 130 digital acquisition system.

We visually examine all the teleseismic data within the epicentral distance range of 30° – 90° from earthquakes with a magnitude between 5.5 and 7.5 that occurred from 10/2006 to 07/2009 (Fig. 1 inset). We choose a total of 384 earthquakes that are well recorded by the North China Array stations. These earthquakes provide ideal coverage in both distance and azimuth.

3. Methodology

3.1. Measuring the frequency-dependent apparent P-wave splitting times

For a teleseismic recording in the epicentral distance range of 30° – 90° , we first rotate the two horizontal components of the seismograms to the radial and transverse components. We then bandpass filter the vertical and horizontal components with a 2-pole Butterworth filter in five difference period bands: 1–10s, 2–20s, 3–30s, 4–40s, and 5–50s. Fig. 3 shows an example of the bandpass filtered seismograms at 1–10s, 3–30s, and 5–50s recorded at the A005 station located inside the Jizhong sub-basin, and their P-wave particle motions, which exhibit a strong non-linear component at all the period bands.

We select data with a signal-to-noise ratio (SNR) ≥ 5 and employ a cross-correlation based method to measure the time lag of the P-wave arrival on the radial component. The cross correlation is computed in the time domain by sliding the radial component to obtain the maximum cross correlation coefficient. We further employ a cosine function to fit the discrete cross correlation function in order to obtain sub-sample delay time measurements [13].

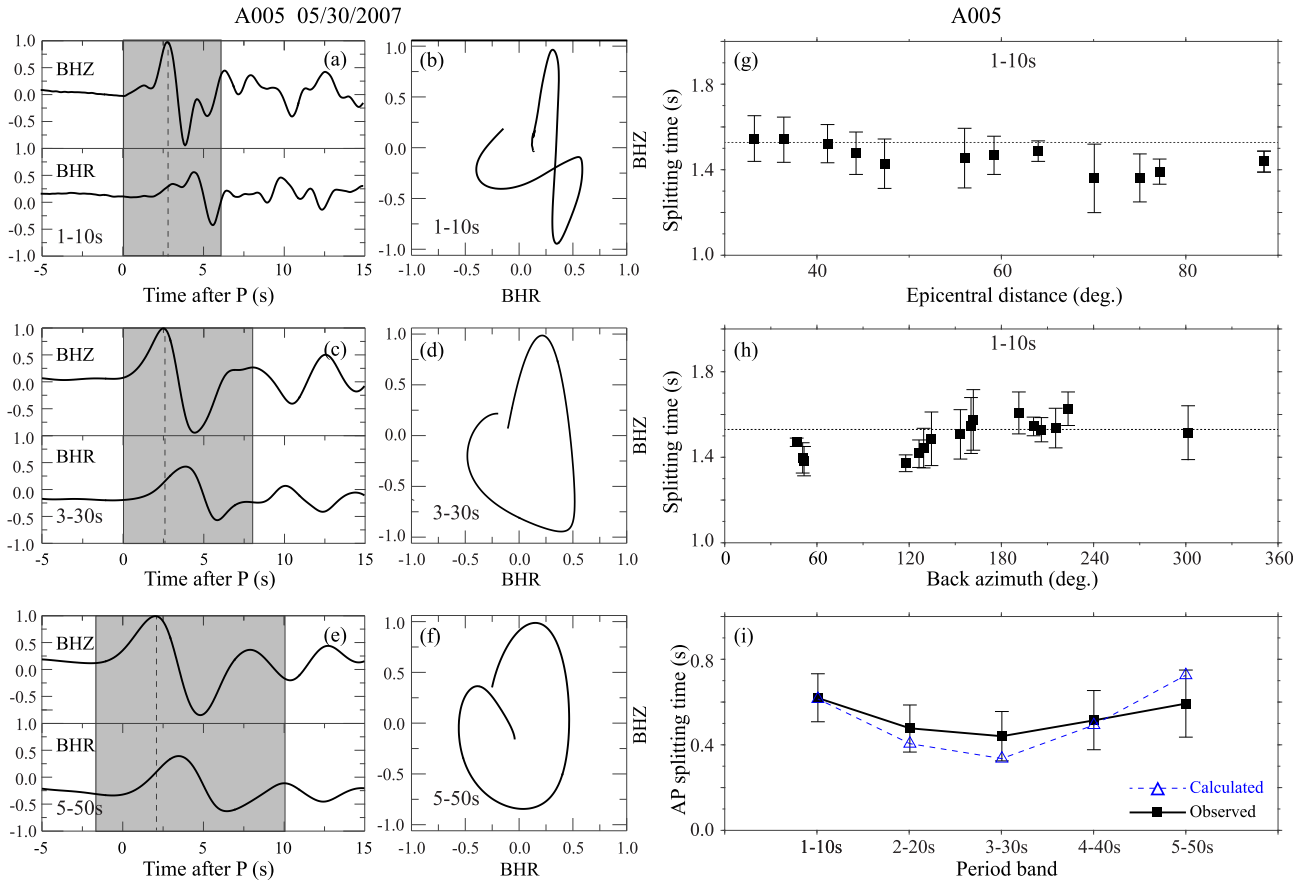


Fig. 3. (a) Normalized vertical- (BHZ) and radial-component (BHR) recordings of A005 located at the Jizhong sub-basin from a teleseismic earthquake occurring on May 30, 2007, which is filtered in the period band of 1–10s. (b) The particle motion of the P wave, which is denoted by the shaded time window in (a). (c) and (d) are similar to (a) and (b), but in the period band of 3–30 s. (e) and (f) are similar to (a) and (b), but for the period band of 5–50s. Note the strong nonlinear particle motion in the 1–10s (b), which changes gradually to nearly linear at 5–50s (f). (g) Measured apparent P-wave splitting times of 92 teleseismic events in the period band of 1–10s are plotted against epicentral distances. The splitting times are averaged ones in a 10-degree bin with error bars indicating the standard deviations. (h) The estimated AP splitting times are shown as a function of event back azimuth. The data are binned in a 20-degree window. (i) The average apparent P-wave splitting time of each period band is plotted as a function of period (black solid squares). Open triangles represent the computed splitting times from the inverted model. Note that the splitting time stays high across all the period bands.

For station A005, the number of earthquakes selected for measurement is 92 at the shortest period band (1–10s) and 74 at the longest period band (5–50s). Due to the thick sediment cover, the P waves recorded by the radial component of the station show very large delay as compared to those on the vertical component. The apparent P-wave splitting times measured from different earthquakes appear to be stable and are independent of epicentral distance (Fig. 3g) and back azimuth (Fig. 3h). The average splitting time is 1.614 ± 0.115 s and 1.586 ± 0.160 s at the shortest period and longest period bands, respectively (Fig. 3i).

3.2. Grid search of sediment thickness and velocity

We use the grid-search technique developed by Bao and Niu [10] to search for the optimum sediment thickness and S-wave velocity that match the observed AP splitting times. We scale the P-wave velocity (α) from S-wave velocity (β) using a linear relationship compiled by Castagna et al. [14] from clastic silicate rocks:

$$\alpha = 1.16\beta + 1.36 \quad (1)$$

We compute density, ρ , from α using the scaling equation obtained by Brocher [15]:

$$\rho(g/cm^3) = 1.6612\alpha - 0.4721\alpha^2 + 0.0671\alpha^3 - 0.0043\alpha^4 + 0.000106\alpha^5 \quad (2)$$

We further assume that shear-wave velocity increases linearly with depth:

$$\beta(z) = \beta_0 + kz, \quad (3)$$

where β_0 is the S-wave velocity at the surface and k is the velocity gradient with respect to the depth ($\delta\beta/\delta z$), which is assumed to be constant here. When k is zero, velocity inside the sediment is constant. We parameterize the sediments with a stack of constant velocity layers with a thickness between 0.2 and 0.4 km. Beneath the sedimentary layer, the crystalline crust is assumed to have a constant P- and S-wave velocity and density, which is 6.4 km/s, 3.46 km/s, and 2.7 g/cm³, respectively. It is underlain by a half-space mantle with a constant $\alpha = 8.0$ km/s, $\beta = 4.5$ km/s and $\rho = 3.3$ g/cm³.

We vary the sediment thickness from Z_{\min} to Z_{\max} and β_0 from $\beta_{0\min}$ to $\beta_{0\max}$ with an increment of $\Delta z = 0.02$ km and $\Delta\beta = 0.01$ km/s, respectively. k is chosen with a try and error approach. For each searched model, we use the Thomson–Haskell

propagator matrix method [16,17] to generate vertical and radial seismograms of all the earthquakes. The incident angle is calculated using the iasp91model [18] based on the epicentral distance and focal depth. The synthetic seismograms are filtered with the same bandpass filters. We then measure the apparent P-wave splitting times from the filtered synthetic seismograms of all the earthquakes and further compute their average. The objective function is taken as the weighted average residual between the observed and calculated AP splitting times:

$$\Delta T = \left[\frac{1}{N} \sum_{i=1}^N \frac{(T_{oi} - T_{ci})^2}{\sigma_{oi}^2} \right]^{\frac{1}{2}} \quad (4)$$

Here N is total number of period bands, which is 5. T_{oi} and T_{ci} are the observed and calculated AP splitting time of the i -th period band, and σ_{oi} is the uncertainty of T_{oi} . The thickness and velocity

ranges are chosen when the average time residual, ΔT , reaches minimum.

4. Results and discussion

4.1. Observed AP splitting times

Fig. 4 shows another example of the nonlinear P-wave particle motions observed at station A010, which is located at the Cangxian uplift of the Bohai Bay basin. The observed apparent P-wave splitting time decreases slightly with increasing period (Fig. 4c), which is slightly different from those observed at A005 (Fig. 3).

We measure the apparent P-wave splitting times at all the 249 stations. The average number of events used in the measurements is 148 at the shortest period band, and decays slightly to 104 at 5–50s. The measured apparent times at the five period bands and their average are listed in Table 1. In Fig. 5, we show

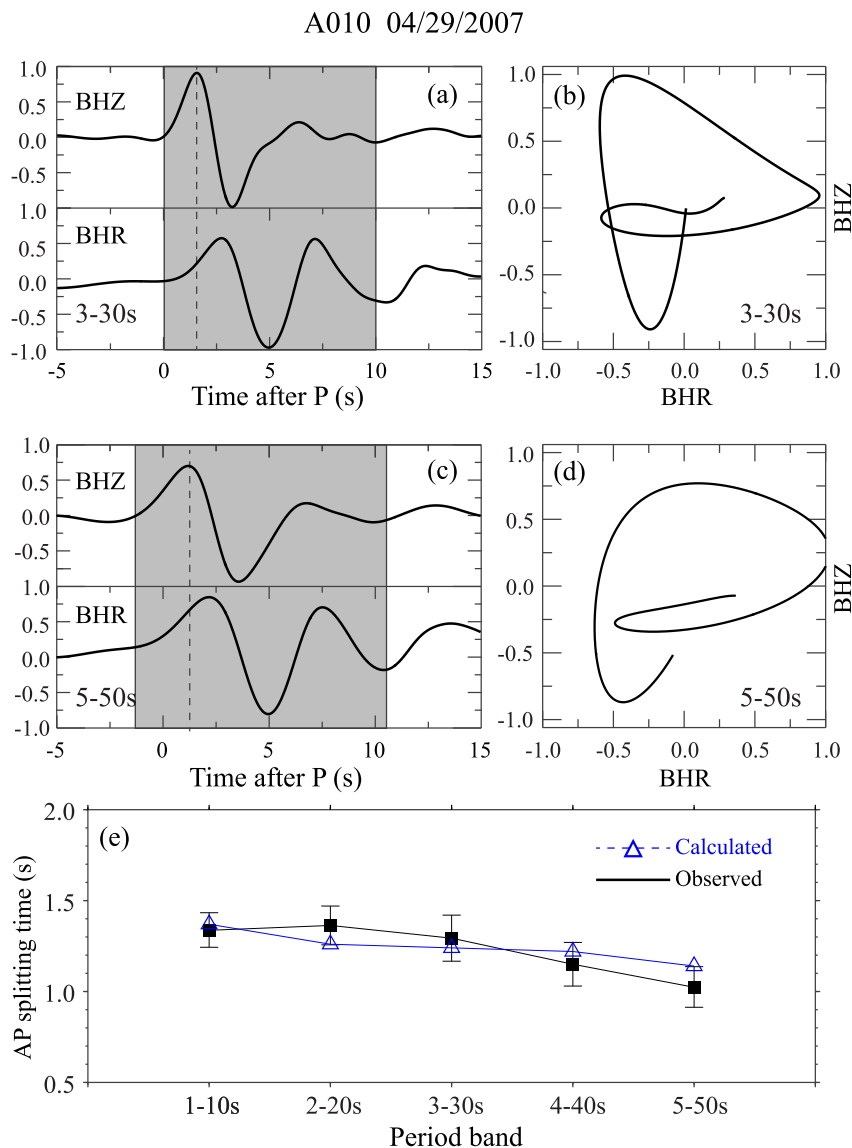


Fig. 4. (a) Normalized vertical- (BHZ) and radial-component (BHR) recordings of A010 on the Cangxian Uplift from a teleseismic earthquake occurring on May 30, 2007, which is filtered in the period band of 3–30s. (b) The particle motion of the P wave, which is denoted by the shaded time window in (a). (c) and (d) are similar to (a) and (b), but in the period band of 5–50 s. (e) The average AP splitting times measured at A010 are plotted as a function of period (black solid squares), which remain roughly flat across all the period bands.

Table 1
Observed AP splitting times and 2D grid search results.

Sta.	Lon. (°)	Lat. (°)	Elev. (km)	AP splitting time (s)					$\delta\beta/\delta z$ ^a	Z (km)	β (km/s)	VR (%)	Z _{2.5} (km) ^b
				1_10s	2_20s	3_30s	4_40s	5_50s					
A410	119.08	39.55	0.011	1.364 ± 0.178	1.427 ± 0.185	1.532 ± 0.174	1.494 ± 0.174	1.456 ± 0.161	0.57	3.02	0.48	94.86	3.02
A613	116.43	40.10	0.036	0.775 ± 0.091	0.641 ± 0.125	0.469 ± 0.136	0.305 ± 0.110	0.213 ± 0.106	1.50	1.02	0.38	88.96	1.02
K033	116.79	40.13	0.027	0.636 ± 0.106	0.562 ± 0.137	0.425 ± 0.143	0.323 ± 0.130	0.288 ± 0.126	1.50	2.04	0.48	86.06	1.35
K040	117.58	39.80	0.008	0.710 ± 0.144	0.580 ± 0.158	0.387 ± 0.132	0.286 ± 0.114	0.263 ± 0.116	1.50	2.04	0.48	83.93	1.35
K041	117.69	39.74	0.005	1.049 ± 0.172	0.944 ± 0.168	0.767 ± 0.177	0.618 ± 0.155	0.511 ± 0.127	1.40	2.16	0.26	87.83	1.60
K042	117.80	39.67	0.007	1.075 ± 0.121	1.005 ± 0.163	0.814 ± 0.173	0.612 ± 0.168	0.498 ± 0.149	1.40	2.40	0.40	88.86	1.50
K043	117.90	39.63	0.002	0.467 ± 0.062	0.398 ± 0.072	0.318 ± 0.089	0.273 ± 0.098	0.271 ± 0.109	1.50	2.00	0.60	74.88	1.27
K044	117.96	39.60	0.008	0.552 ± 0.088	0.508 ± 0.102	0.399 ± 0.111	0.303 ± 0.101	0.273 ± 0.094	1.50	1.64	0.52	83.68	1.32
K045	118.05	39.54	0.007	0.737 ± 0.095	0.673 ± 0.121	0.507 ± 0.122	0.386 ± 0.103	0.334 ± 0.093	1.50	2.04	0.42	87.89	1.39
K046	118.17	39.51	0.006	0.722 ± 0.093	0.674 ± 0.111	0.557 ± 0.123	0.450 ± 0.125	0.388 ± 0.125	1.50	2.06	0.40	85.99	1.40
K047	118.31	39.46	0.008	1.213 ± 0.105	1.258 ± 0.130	1.153 ± 0.175	0.972 ± 0.167	0.821 ± 0.142	0.57	4.42	0.66	90.73	3.23
K048	118.42	39.41	0.004	1.401 ± 0.254	1.442 ± 0.203	1.258 ± 0.208	1.030 ± 0.191	0.877 ± 0.126	0.57	4.00	0.56	95.25	3.40
K049	118.53	39.35	0.004	1.393 ± 0.133	1.361 ± 0.163	1.505 ± 0.210	1.548 ± 0.185	1.530 ± 0.164	0.57	3.00	0.46	94.43	3.00
K051	118.74	39.25	0.003	1.268 ± 0.322	1.446 ± 0.252	1.443 ± 0.281	1.401 ± 0.233	1.348 ± 0.248	0.57	3.08	0.50	92.89	3.08
S102	117.77	39.45	0.003	1.534 ± 0.241	1.671 ± 0.268	1.668 ± 0.199	1.438 ± 0.207	1.260 ± 0.191	0.57	5.24	0.48	92.02	3.54
S104	117.86	39.50	0.003	1.028 ± 0.058	1.156 ± 0.107	1.201 ± 0.090	1.088 ± 0.161	0.957 ± 0.183	0.57	3.16	0.64	90.03	3.16
S105	117.91	39.54	0.004	0.951 ± 0.077	1.016 ± 0.075	0.894 ± 0.124	0.714 ± 0.159	0.561 ± 0.178	0.57	4.42	0.82	83.85	2.95
S108	117.97	39.71	0.007	1.002 ± 0.247	0.976 ± 0.145	0.859 ± 0.135	0.725 ± 0.141	0.611 ± 0.156	0.57	4.42	0.82	87.29	2.95
S109	117.96	39.47	0.004	1.108 ± 0.074	1.207 ± 0.113	1.193 ± 0.136	1.036 ± 0.173	0.877 ± 0.177	0.57	4.42	0.66	90.48	3.23
S110	118.02	39.40	0.002	1.281 ± 0.067	1.346 ± 0.084	1.367 ± 0.079	1.269 ± 0.097	1.137 ± 0.118	0.57	4.00	0.56	94.42	3.40
S111	118.24	39.27	0.003	1.114 ± 0.522	1.679 ± 0.301	1.696 ± 0.180	1.549 ± 0.145	1.405 ± 0.140	0.57	3.12	0.46	84.85	3.12
S113	118.13	39.45	0.004	1.107 ± 0.096	1.145 ± 0.103	1.160 ± 0.104	1.038 ± 0.136	0.876 ± 0.169	0.57	4.42	0.66	92.22	3.23
S116	118.12	39.34	0.003	1.438 ± 0.060	1.528 ± 0.094	1.528 ± 0.066	1.512 ± 0.069	1.495 ± 0.075	0.57	3.12	0.46	95.67	3.12
S118	118.21	39.45	0.005	1.040 ± 0.125	1.193 ± 0.120	1.168 ± 0.137	1.008 ± 0.153	0.849 ± 0.175	0.57	4.58	0.68	88.82	3.19
S121	118.28	39.38	0.004	1.364 ± 0.031	1.388 ± 0.111	1.369 ± 0.071	1.370 ± 0.100	1.315 ± 0.094	0.57	3.62	0.52	96.69	3.47
S126	118.41	39.58	0.022	0.647 ± 0.070	0.572 ± 0.078	0.442 ± 0.094	0.325 ± 0.114	0.258 ± 0.114	1.50	2.04	0.48	89.16	1.35
S128	118.49	39.46	0.014	1.053 ± 0.147	1.150 ± 0.152	1.214 ± 0.126	1.069 ± 0.154	0.906 ± 0.184	0.57	4.42	0.66	90.20	3.23
S135	118.62	39.50	0.018	0.929 ± 0.082	0.976 ± 0.122	0.880 ± 0.160	0.653 ± 0.189	0.475 ± 0.202	1.40	2.40	0.30	92.36	1.57
S139	118.76	39.56	0.015	0.934 ± 0.062	0.907 ± 0.123	0.798 ± 0.151	0.598 ± 0.186	0.450 ± 0.190	1.40	2.40	0.32	93.65	1.56
A006	115.98	38.07	0.017	1.516 ± 0.179	1.349 ± 0.229	1.354 ± 0.253	1.429 ± 0.208	1.510 ± 0.186	0.57	3.72	0.50	93.98	3.51
A008	116.19	38.29	0.013	1.325 ± 0.603	1.136 ± 0.656	1.045 ± 0.652	1.043 ± 0.657	1.152 ± 0.703	0.57	5.16	0.62	92.98	3.30
A010	116.30	37.86	0.016	1.338 ± 0.094	1.363 ± 0.107	1.292 ± 0.126	1.151 ± 0.120	1.024 ± 0.112	0.57	4.42	0.56	93.50	3.40
A011	116.50	38.05	0.013	1.332 ± 0.084	1.381 ± 0.118	1.346 ± 0.141	1.220 ± 0.151	1.093 ± 0.162	0.57	4.84	0.56	94.55	3.40
A012	116.54	38.54	0.009	1.419 ± 0.093	1.346 ± 0.133	1.322 ± 0.145	1.224 ± 0.154	1.105 ± 0.141	0.57	4.82	0.56	96.52	3.40
A013	116.67	38.21	0.012	1.264 ± 0.156	1.227 ± 0.153	1.070 ± 0.189	0.847 ± 0.203	0.697 ± 0.177	0.57	4.58	0.68	84.41	3.19
A014	116.89	38.42	0.007	1.463 ± 0.064	1.451 ± 0.094	1.433 ± 0.128	1.423 ± 0.142	1.339 ± 0.169	0.57	3.80	0.50	98.22	3.51
A705	116.79	38.79	0.004	1.497 ± 0.071	1.495 ± 0.104	1.377 ± 0.157	1.200 ± 0.170	1.044 ± 0.159	0.57	4.82	0.54	91.28	3.44
A711	117.26	38.80	0.006	1.518 ± 0.059	1.470 ± 0.056	1.478 ± 0.089	1.478 ± 0.095	1.437 ± 0.106	0.57	3.62	0.48	98.40	3.54
A712	117.47	39.49	0.003	1.587 ± 0.202	1.607 ± 0.106	1.639 ± 0.195	1.680 ± 0.220	1.696 ± 0.216	0.57	3.08	0.42	96.05	3.08
A713	117.42	38.97	0.001	1.382 ± 0.087	1.427 ± 0.169	1.355 ± 0.136	1.251 ± 0.137	1.156 ± 0.132	0.57	4.84	0.56	95.25	3.40
A715	117.83	39.39	0.004	1.387 ± 0.064	1.425 ± 0.056	1.427 ± 0.089	1.378 ± 0.117	1.310 ± 0.129	0.57	4.12	0.52	96.31	3.47
L231	115.85	37.72	0.021	1.417 ± 0.129	1.257 ± 0.123	1.278 ± 0.134	1.355 ± 0.175	1.454 ± 0.189	0.57	3.22	0.52	93.20	3.22
L232	115.98	37.68	0.021	1.358 ± 0.077	1.353 ± 0.116	1.353 ± 0.116	1.318 ± 0.119	1.266 ± 0.123	0.57	4.00	0.54	97.08	3.44
L233	116.10	37.61	0.017	1.405 ± 0.123	1.431 ± 0.150	1.344 ± 0.122	1.262 ± 0.116	1.194 ± 0.121	0.57	4.82	0.54	96.37	3.44
S101	117.68	39.35	0.003	1.674 ± 0.062	1.554 ± 0.251	1.527 ± 0.193	1.630 ± 0.138	1.648 ± 0.113	0.57	3.52	0.44	95.52	3.52
S107	117.93	39.34	0.000	1.552 ± 0.033	1.490 ± 0.151	1.554 ± 0.106	1.493 ± 0.111	1.441 ± 0.155	0.57	3.36	0.46	98.16	3.36
A802	113.21	39.98	1.032	1.415 ± 0.109	1.521 ± 0.128	1.559 ± 0.147	1.532 ± 0.152	1.506 ± 0.141	0.57	3.12	0.46	95.24	3.12
A803	113.26	39.58	1.007	1.235 ± 0.458	0.967 ± 0.325	0.879 ± 0.243	0.743 ± 0.217	0.604 ± 0.181	1.40	2.60	0.32	87.63	1.56
A805	113.46	39.85	0.980	0.924 ± 0.178	0.967 ± 0.366	0.913 ± 0.318	0.693 ± 0.242	0.509 ± 0.184	1.40	2.40	0.30	90.72	1.57
A808	113.72	39.73	1.123	0.526 ± 0.104	0.482 ± 0.096	0.411 ± 0.111	0.315 ± 0.109	0.238 ± 0.100	1.50	2.12	0.54	84.56	1.31
A809	113.81	39.96	0.984	0.668 ± 0.226	0.624 ± 0.160	0.590 ± 0.135	0.498 ± 0.138	0.428 ± 0.131	0.57	3.22	1.00	88.13	2.63
L210	112.73	39.24	1.077	0.815 ± 0.552	1.050 ± 0.423	1.017 ± 0.198	0.929 ± 0.159	0.854 ± 0.132	0.57	3.14	0.72	84.95	3.12
A709	117.11	38.60	0.004	1.884 ± 0.101	1.827 ± 0.112	1.750 ± 0.131	1.789 ± 0.158	1.829 ± 0.186	0.57	4.26	0.38	96.72	3.72
S106	117.90	39.23	0.003	1.873 ± 0.071	1.835 ± 0.026	1.811 ± 0.038	1.777 ± 0.065	1.725 ± 0.071	0.57	4.32	0.38	99.56	3.72
L236	116.56	37.39	0.019	1.262 ± 0.296	1.476 ± 0.322	1.506 ± 0.173	1.415 ± 0.135	1.316 ± 0.135	0.57	3.08	0.50	91.93	3.08
VDSH	117.68	38.01	0.017	1.150 ± 0.092	1.189 ± 0.133	1.143 ± 0.229	1.003 ± 0.216	0.797 ± 0.233	0.57	4.58	0.68	90.26	3.19
A001	115.23	38.47	0.040	1.562 ± 0.079	1.466 ± 0.111	1.448 ± 0.142	1.555 ± 0.177	1.667 ± 0.197	0.57	3.22	0.46	93.16	3.22
A002	115.35	38.69	0.027	1.762 ± 0.168	1.715 ± 0.141	1.683 ± 0.120	1.672 ± 0.127	1.657 ± 0.129	0.57	3.62	0.40	98.02	3.62
A003	115.59	38.21	0.021	1.587 ± 0.167	1.411 ± 0.155	1.288 ± 0.123	1.332 ± 0.156	1.455 ± 0.185	0.57	4.46	0.50	93.26	3.51
A004	115.73	38.83	0.010	1.523 ± 0.188	1.435 ± 0.191	1.460 ± 0.201	1.549 ± 0.206	1.675 ± 0.189	0.57	3.22	0.46	92.87	3.22
A005	115.73	38.52	0.018	1.614 ± 0.115	1.468 ± 0.113	1.432 ± 0.117	1.507 ± 0.141	1.586 ± 0.160	0.57	3.58	0.46	94.62	3.58
A007	116.05	38.91	0.010	1.490 ± 0.056	1.439 ± 0.052	1.405 ± 0.080	1.409 ± 0.093	1.389 ± 0.117	0.57	3.80	0.50	98.04	3.51
A009	116.20	38.65	0.008	1.506 ± 0.173	1.456 ± 0.225	1.419 ± 0.280	1.504 ± 0.231	1.542 ± 0.226	0.57	3.46	0.48	94.98	3.46
A701	116.08	39.16	0.017	1.325 ± 0.417	1.507 ± 0.214	1.647 ± 0.251	1.625 ± 0.223	1.586 ± 0.216	0.57	3.04	0.44	92.12	3.04
A702	116.41	39.52	0.026	1.462 ± 0.128	1.465 ± 0.133	1.470 ± 0.198	1.380 ± 0.159	1.266 ± 0.151	0.57	4.02	0.50	96.63	3.51
A703	116.42	39.00	0.004	1.750 ± 0.144	1.630 ± 0.169	1.495 ± 0.160	1.460 ± 0.188	1.541 ± 0.230	0.57	5.48	0.46	95.39	3.58
A704	116.73	39.85	0.020	0.879 ± 0.137	0.768 ± 0.165	0.641 ± 0.188	0.491 ± 0.165	0.369 ± 0.166	1.50	2.00	0.34	89.58	1.44
A706	116.85	39.35	0.012	1.778 ± 0.231	1.741 ± 0.201	1.583 ± 0.208	1.521 ± 0.221	1.573 ± 0.264	0.57	5.22	0.44	96.04	3.61
A707	116.86	39.10											

Table 1 (continued)

Sta.	Lon. (°)	Lat. (°)	Elev. (km)	AP splitting time (s)					$\delta\beta/\delta z$ ^a	Z (km)	β (km/s)	VR (%)	$Z_{2.5}$ (km) ^b
				1_10s	2_20s	3_30s	4_40s	5_50s					
L226	115.02	38.14	0.043	1.485 ± 0.102	1.385 ± 0.088	1.371 ± 0.084	1.412 ± 0.096	1.442 ± 0.114	0.57	3.72	0.50	96.28	3.51
L227	115.21	38.06	0.036	1.381 ± 0.145	1.234 ± 0.123	1.188 ± 0.096	1.190 ± 0.104	1.199 ± 0.115	0.57	5.50	0.58	97.14	3.37
L228	115.39	37.96	0.030	1.216 ± 0.387	1.190 ± 0.326	1.114 ± 0.359	1.161 ± 0.355	1.310 ± 0.326	0.57	3.42	0.58	90.79	3.37
L229	115.57	37.88	0.027	1.390 ± 0.205	1.267 ± 0.193	1.161 ± 0.217	1.119 ± 0.257	1.243 ± 0.267	0.57	5.42	0.58	94.15	3.37
L230	115.71	37.80	0.021	1.548 ± 0.111	1.358 ± 0.186	1.319 ± 0.217	1.338 ± 0.279	1.451 ± 0.299	0.57	3.78	0.50	94.00	3.51
VWEA	116.45	38.85	0.004	1.583 ± 0.098	1.549 ± 0.121	1.541 ± 0.121	1.564 ± 0.130	1.584 ± 0.147	0.57	3.36	0.44	96.81	3.36
L234	116.26	37.54	0.021	1.535 ± 0.052	1.528 ± 0.078	1.494 ± 0.097	1.461 ± 0.106	1.455 ± 0.111	0.57	4.24	0.48	97.47	3.54
L235	116.41	37.47	0.022	1.778 ± 0.157	1.699 ± 0.126	1.595 ± 0.109	1.605 ± 0.124	1.662 ± 0.143	0.57	4.58	0.42	96.68	3.65
A602	114.94	40.00	0.939	0.880 ± 0.108	0.786 ± 0.120	0.627 ± 0.146	0.464 ± 0.165	0.340 ± 0.160	1.50	2.28	0.34	90.34	1.44
A605	115.25	40.37	0.522	1.138 ± 0.167	1.181 ± 0.124	1.143 ± 0.134	1.036 ± 0.153	0.879 ± 0.168	0.57	4.42	0.66	92.55	3.23
K005	113.59	41.48	1.367	0.699 ± 0.139	0.671 ± 0.155	0.654 ± 0.192	0.556 ± 0.186	0.423 ± 0.166	0.57	4.96	1.00	89.33	2.63
K006	113.67	41.44	1.342	0.818 ± 0.136	0.839 ± 0.151	0.760 ± 0.161	0.639 ± 0.158	0.528 ± 0.143	0.57	4.42	0.90	87.31	2.81
K007	113.77	41.40	1.370	0.832 ± 0.082	0.787 ± 0.116	0.746 ± 0.134	0.657 ± 0.162	0.560 ± 0.173	0.57	4.42	0.90	91.23	2.81
K008	113.86	41.36	1.341	0.681 ± 0.173	0.623 ± 0.115	0.502 ± 0.131	0.376 ± 0.136	0.267 ± 0.125	1.50	1.82	0.44	90.78	1.37
A508	114.59	40.14	0.992	0.514 ± 0.099	0.396 ± 0.081	0.315 ± 0.100	0.234 ± 0.107	0.191 ± 0.103	1.50	2.00	0.62	83.48	1.25
A301	117.62	40.56	0.555	0.397 ± 0.500	0.399 ± 0.554	0.386 ± 0.582	0.351 ± 0.546	0.374 ± 0.557	1.50	2.00	0.60	62.14	1.27
K015	114.69	41.06	1.468	0.563 ± 0.090	0.453 ± 0.112	0.306 ± 0.102	0.233 ± 0.088	0.171 ± 0.083	1.50	2.00	0.60	86.10	1.27
K026	116.01	40.46	0.488	0.623 ± 0.094	0.463 ± 0.102	0.308 ± 0.100	0.214 ± 0.099	0.160 ± 0.096	1.50	1.02	0.50	84.74	1.02

^a (km/s)/km.

^b Sediment thickness with a base S-wave velocity of 2.5 km/s.

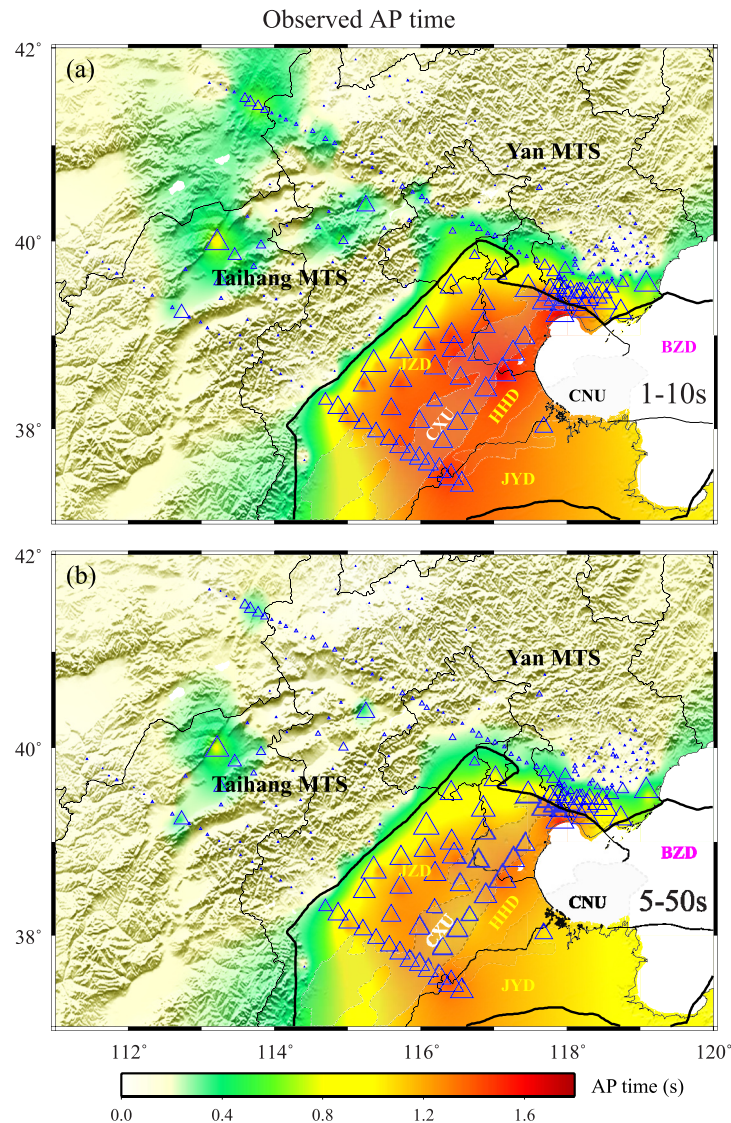


Fig. 5. Apparent P-wave splitting times estimated from the 48 stations within the Bohai Bay basin and other 42 stations with significant P-wave delay on the radial component. Measurements are made at period band of 1–10 s (a) and 5–50s (b).

the measured splitting times from the shortest period band (Fig. 5a) and the longest period band (Fig. 5b). In general, the apparent P-wave splitting times measured at 1–10s are slightly larger than those computed at 5–50s. It is very clear that stations inside the Bohai Bay basin show the largest splitting times in all the five period bands. There is a sharp reduction in the splitting time at the western and northern edge of the basin. The western boundary matches well with the geologically defined boundary of the basin (thick solid black line in Fig. 5), which we digitized from Yang and Badal [1]. However, it seems that the area with large apparent splitting time extend further north than the northern boundary, but much less in the northwest direction (Fig. 5).

Stations located at the Taihang and Yanshan Mountains ranges generally show no significant ($< \sim 0.3$ s) apparent P-wave splitting. There are a few stations located within the two mountain ranges that have significant splitting times. These stations seem to be inside the local basins within the two ranges, such as the Datong Basin (DTB) of the Taihang range.

4.2. Grid search results

We select a total of 90 stations with an average splitting time of greater than 0.3 s. Following Bao and Niu [10], we employ three thickness/velocity ranges and velocity-depth slopes with a thin, moderately thick, and thick sedimentary layer, respectively, in searching the optimum sedimentary structure beneath each station. Fig. 6 shows two examples of the grid search results at stations K008 and A005, which are underlain by a moderately thick and a thick sedimentary layer, respectively. Both stations show a reasonably well defined (Z_0, β_0) that gives the minimum misfit, although the resolution of Z_0 is slightly low.

The obtained thickness and surface S-wave velocity are listed in Table 1. The variance reduction varies from 62.14% to 99.56% with an average value of 91.70%. We further employ an inversion scheme to interpolate the measurements at the 90 stations to a $0.1^\circ \times 0.1^\circ$ regular grid [19]. The calculated sediment thickness is shown in Fig. 7a. Bao and Niu [10] found that the sediment thickness estimated from the grid search could be significantly affected by the crystalline crustal model employed in computing synthetics, while the thickness of the layer with a bottom S-wave velocity of 2.5 km/s ($Z_{2.5}$) appears to be almost insensitive to the reference crystalline crustal model. Thus we recompute the sediment thickness defined by $Z_{2.5}$ beneath each station. We use equation (3) to compute $Z_{2.5}$. If $Z_{2.5}$ is larger than the grid-search based depth, which means that S-wave velocity inside the entire sedimentary layer is less than 2.5 km/s, then we take the grid-search based sediment thickness. The interpolated $Z_{2.5}$ is shown in Fig. 7b.

We have a total of 48 broadband stations inside the Bohai Bay basin outlined by the thick solid line. The computed $Z_{2.5}$ varies from 1.02 km to 3.72 km, with an average of 3.20 km. Among the 48 stations, 17 stations are located inside the Cangxian uplift and 22 stations are inside the Jizhong depression. There is no significant difference in sediment thickness computed from the two geological units.

Zhao and Zheng [20] modeled waveforms of S wave and the following sediment reverberations of three teleseismic events recorded by a 1-D broadband seismic array deployed across the Bohai Bay basin. They obtained the S-wave velocity structure of the sediments beneath the array, which shows a good spatial correlation with sub-basin structures. The sediment is approximately 2 km thick beneath the Cangxian uplift located in the central part of the Bohai Bay basin, and deepens sharply toward westward, which reaches to nearly 4 km deep beneath the

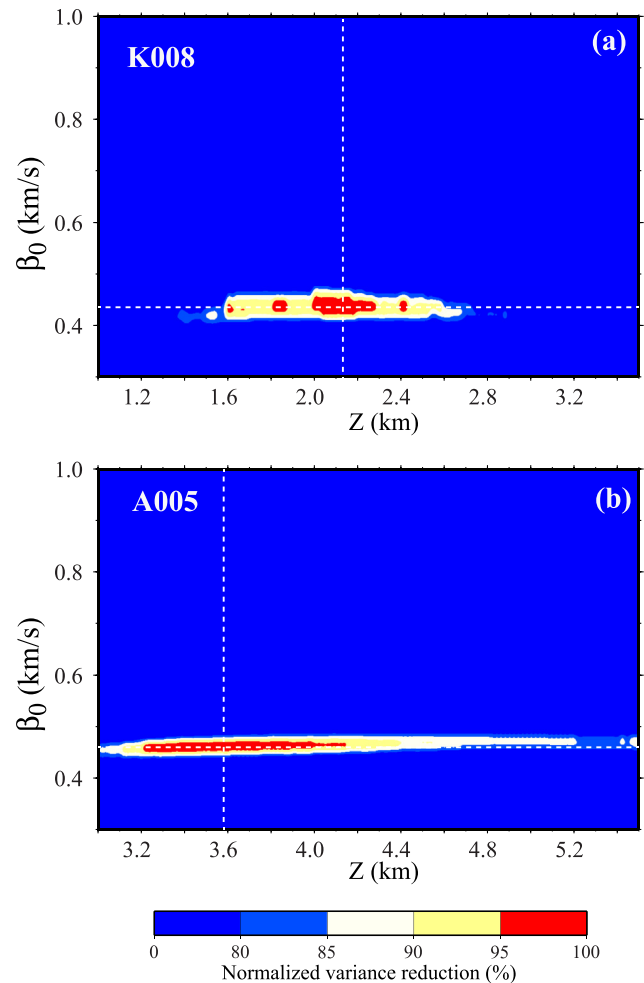


Fig. 6. (a) The 2D grid search result computed from the apparent P-wave splitting times measured at station K008, which is underlain by a moderately thick sediment layer. The normalized variance reduction is indicated by color contour map in which “hotter” color clusters represent greater variance reduction. The two thin white dashed lines indicate the optimum sediment thickness and surface S-wave velocity at which the variance reduction reaches the maximum. (b) Same as (a) except for station A005.

Jizhong depression. Our measurements of the sediment thickness beneath the Jizhong depression agree well with their observations. However, our measurements do not show significant difference between stations located at the Cangxian uplift and the Jizhong depression (Fig. 5). Overall the estimated sediment thickness beneath the northwestern section of the basin is rather uniform. This might be due to the sparse distribution of seismic stations inside the basin except for the southern K line. Another possibility is that the Cangxian uplift is a much smaller structure inside the basin. We also notice that area with significantly thick sediment extends further north to the known boundary of the basin.

5. Conclusions

The teleseismic P wave field recorded by a broadband seismic array deployed within the western part of the Bohai Bay basin shows significant and frequency dependent delays on the radial component, which is caused by interference from the sediment reverberations. We employ a grid-search technique to estimate sediment thickness and S-wave velocity at surface that best

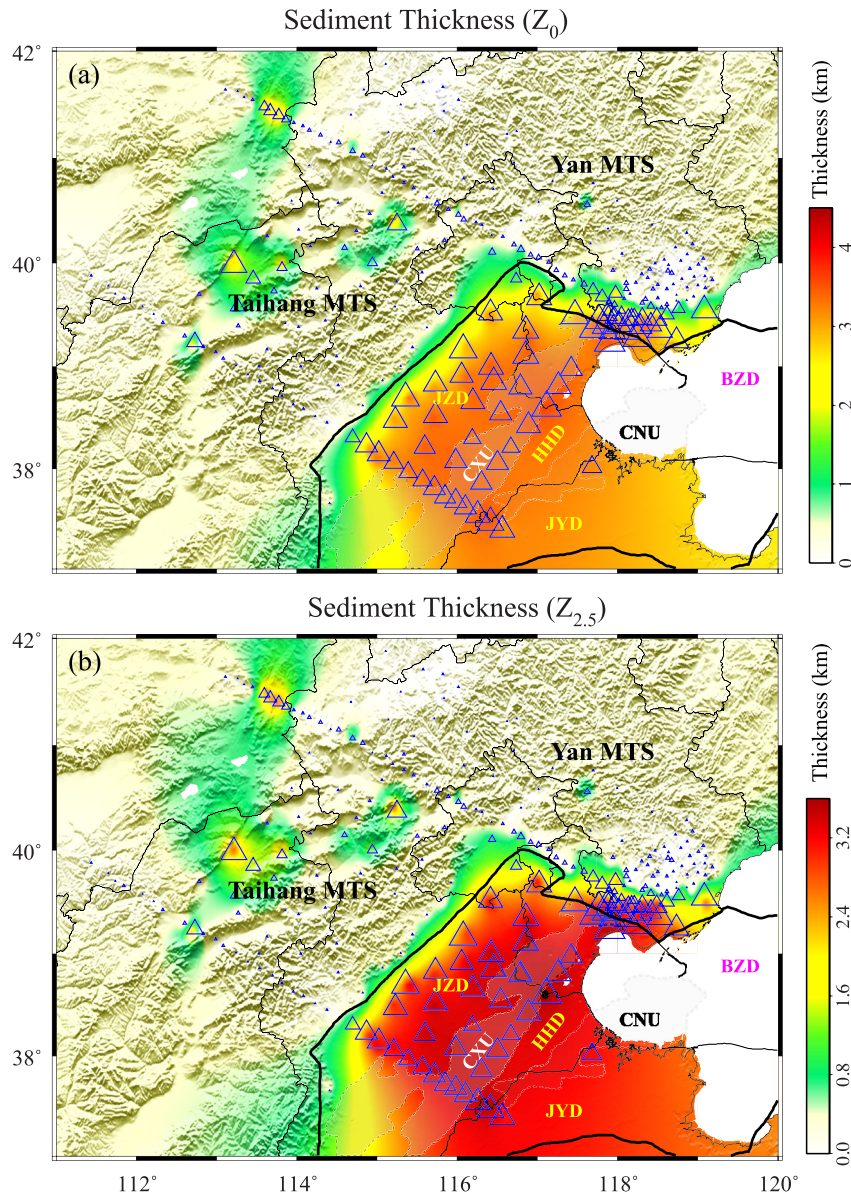


Fig. 7. Map showing the inverted sediment thickness from the 2D grid search (a) and sediment thickness defined by a base S-wave velocity of 2.5 km/s (b).

matches the observed delay times. The inverted thickness of the sedimentary layer beneath the northwestern part of the basin varies from 1.02 km to 3.72 km with an average of 3.20 km. It seems that sediments are evenly distributed across large part of the basin, and the layer does not thin significantly beneath the Cangxian uplift. Our measurements also indicate that the western boundary between the basin and the Taihang Mountains is rather sharp and generally agrees with the known western borderline of the Bohai Bay basin, while the northern border of the basin in our study seems to extend further north.

Acknowledgements

We thank the Project of North China Array of the China Earthquake Administration for providing the waveform data. We are grateful to the guest editor, Dr. Lanbo Liu, and two anonymous reviewers for their constructive comments and suggestions, which significantly improved the quality of this paper. This study is supported by NSF EAR-1547228.

References

- [1] L. Yang, J. Badal, Mirror symmetry of the crust in the oil/gas region of Shengli, China, *J. Asian Earth Sci.* 78 (2013) 327–344.
- [2] D. McKenzie, Some remarks on the development of sedimentary basins, *Earth Planet. Sci. Lett.* 40 (1978) 25–32, [https://doi.org/10.1016/0012-821X\(78\)90071-7](https://doi.org/10.1016/0012-821X(78)90071-7).
- [3] A. Yin, X. Yu, Z.-K. Shen, J. Liu-Zeng, A possible seismic gap and high earthquake hazard in the North China Basin, *Geology* 43 (2015) 19–22.
- [4] K.B. Olsen, R.J. Archuleta, J.R. Matarese, Three-dimensional simulation of a magnitude 7.75 earthquake on the San Andreas fault in southern California, *Science* 270 (1995) 1628–1632.
- [5] S.-J. Lee, H.-W. Chen, B.-S. Huang, Simulations of strong ground motion and 3D amplification effect in the Taipei basin by using a composite grid finite-difference method, *Bull. Seismol. Soc. Am.* 98 (2008) 1229–1242, <https://doi.org/10.1785/0120060098>.
- [6] R. Taborda, J. Bielak, Ground-motion simulation and validation of the 2008 Chino Hills, California, earthquake, *Bull. Seismol. Soc. Am.* 103 (2013) 131–156, <https://doi.org/10.1785/0120110325>.
- [7] T.J. Owens, R.S. Crosson, Shallow structure effects on broadband teleseismic P waveforms, *Bull. Seismol. Soc. Am.* 78 (1988) 96–108.
- [8] C.A. Langston, Wave-field continuation and decomposition for passive seismic imaging under deep unconsolidated sediments, *Bull. Seismol. Soc. Am.* 101 (2011) 2176–2190.

- [9] K. Tao, F. Niu, J. Ning, Y.J. Chen, S. Grand, H. Kawakatsu, et al., Crustal structure beneath NE China imaged by NECESSArray receiver function data, *Earth Planet. Sci. Lett.* 398 (2014) 48–57.
- [10] Y. Bao, F. Niu, Constraining sedimentary structure using frequency dependent P wave particle motion: a case study of the Songliao Basin in NE China, *J. Geophys. Res.* 122 (2017), <https://doi.org/10.1002/2017JB014721>.
- [11] L.H. Fang, J.P. Wu, Z.Y. Lu, Rayleigh wave group velocity tomography from ambient seismic noise in north China, China, *J. Geophys. Chin. Edn.* 52 (3) (2009) 663–671.
- [12] L.Y. Lu, Z.Q. He, Z.F. Ding, Z.X. Yao, Investigation of ambient noise source in North China array, *Chin. J. Geophys. Ed.* 52 (5) (2009) 1053–1060.
- [13] F. Niu, P. Silver, T. Daley, X. Cheng, E. Majer, Preseismic velocity changes observed from active source monitoring at the Parkfield SAFOD drill site, *Nature* 454 (2008), <https://doi.org/10.1038/nature07111>.
- [14] J.P. Castagna, M.L. Batzle, R.L. Eastwood, Relationships between compressional-wave and shear-wave velocities in clastic silicate rocks, *Geophysics* 50 (1985) 571–581.
- [15] T.M. Brocher, Empirical relations between elastic wavespeeds and density in the Earth's crust, *Bull. Seismol. Soc. Am.* 95 (6) (2005) 2081–2092.
- [16] W.T. Thomson, Transmission of elastic waves through a stratified solid medium, *J. Appl. Phys.* 21 (1950) 89–93.
- [17] N.A. Haskell, Crustal reflection of plane P and SV waves, *J. Geophys. Res.* 67 (1962) 4751–4767.
- [18] B. Kennett, E.R. Engdahl, Travel times for global earthquake location and phase identification, *Geophys. J. Int.* 105 (1991) 429–465.
- [19] F. Niu, T. Baldwin, G. Pavlis, F. Vernon, H. Rendon, M. Bezada, A. Levander, Receiver function study of the crustal structure of the southeastern Caribbean Plate Boundary and Venezuela, *J. Geophys. Res.* 112 (2007) B11308, <https://doi.org/10.1029/2006JB004802>.
- [20] L. Zhao, T. Zheng, Using shear wave splitting measurements to investigate the upper mantle anisotropy beneath the North China Craton: distinct variation from east to west, *Geophys. Res. Lett.* 32 (2005) L10309, <https://doi.org/10.1029/2005GL022585>.



Chenhao Yang is a PhD student at the Department of Earth, Environmental and Planetary Sciences of Rice University. His research involves developing new techniques for better imaging seismic structure of sediment, crust and upper mantle using passive sources, as well employing time-lapse seismic imaging to monitor subsurface structural changes associated with tectonic and environmental processes.



Fenglin Niu is a global seismologist with a primary interest in Earth's deep structure. He got his Ph.D. from the University of Tokyo, Japan. He has been developing imaging techniques to map seismic heterogeneities of Earth's interior at various scales to better understand fundamental chemical and physical processes within the planet. Recently he has also developed a strong interest in understanding earthquake physics, especially in developing seismic imaging techniques for monitoring the subsurface stress field along major faults.